

Journal of Materials Chemistry A

Accepted Manuscript



This is an *Accepted Manuscript*, which has been through the Royal Society of Chemistry peer review process and has been accepted for publication.

Accepted Manuscripts are published online shortly after acceptance, before technical editing, formatting and proof reading. Using this free service, authors can make their results available to the community, in citable form, before we publish the edited article. We will replace this *Accepted Manuscript* with the edited and formatted *Advance Article* as soon as it is available.

You can find more information about *Accepted Manuscripts* in the [Information for Authors](#).

Please note that technical editing may introduce minor changes to the text and/or graphics, which may alter content. The journal's standard [Terms & Conditions](#) and the [Ethical guidelines](#) still apply. In no event shall the Royal Society of Chemistry be held responsible for any errors or omissions in this *Accepted Manuscript* or any consequences arising from the use of any information it contains.

COMMUNICATION

Engineering Crystalline Structures of Two-Dimensional MoS₂ Sheets for High-Performance Organic Solar Cells

Cite this: DOI: 10.1039/x0xx00000x

Xi Yang,^{†a} Weifei Fu,^{†a} Wenqing Liu,^a Jinghua Hong,^c Yu Cai,^a Chuanhong Jin,^c Mingsheng Xu,^{*a} Haibo Wang^b, Deren Yang^d and Hongzheng Chen^{*a}Received 00th January 2012,
Accepted 00th January 2012

DOI: 10.1039/x0xx00000x

www.rsc.org/

The effects of different local crystalline structures in two-dimensional (2D) MoS₂ sheets are studied to provide new insights into how these local characteristics affect the performance of organic solar cells (OSCs) and how to tailor the local characteristics towards high-performance devices. UV-ozone post-treatment of 2D MoS₂ sheets led to incorporation of oxygen atoms into the lattice of the sheets. The incorporated oxygen in 2D MoS₂ sheets significantly improved the performance of OSCs, where 2D MoS₂ sheets were used as a hole transport layer.

Graphene-like two-dimensional (2D) materials such as transition metal dichalcogenides (TMDs) are currently subject of intense research because of their unique electronic structures.¹⁻⁵ Molybdenum disulfide (MoS₂) is one of the prototypical TMD materials. A single layer MoS₂ consists of two planes of hexagonally arranged sulfur (S) atoms linked to a hexagonal plane of molybdenum (Mo) atoms *via* covalent bonds and in its pristine bulk form the individual layers are held together by weak van der Waals forces.⁶ Crystals of MoS₂ can be easily cleaved along the layer plane due to weak van der Waals forces between the layers, which converts the bulk MoS₂ from an indirect band gap semiconductor with an energy gap of about 1.2 eV to a direct band gap of monolayer MoS₂ with an energy gap of about 1.9 eV.^{7,8} MoS₂ displays many intriguing physical and chemical properties¹ with a wide range of potential

applications including in dry lubrication,⁹ hydrogen evolution,¹⁰⁻¹² photovoltaics,^{13,14} light-emitting devices,¹⁵ and photodetectors.¹⁶

Among the methods for synthesis of 2D MoS₂ sheets,¹ lithium intercalation, a scalable and solution process, is a simple method to produce single layer of MoS₂ sheets, where Li-intercalated MoS₂ (Li_xMoS₂) can be exfoliated into monolayers *via* forced hydration, yielding a stable colloidal suspension.^{8,17,18} At present, all the methods cannot produce large-scale MoS₂ sheets with perfect crystalline structures.^{19,20} In fact, there are several reports on the observation of different intrinsic structural defects and various phases mixed with a semiconducting prismatic 2H-phase and a metallic octahedral 1T-phase in monolayer MoS₂ sheets.¹⁹⁻²² The lithium intercalation process is more prone to induce modification of the crystalline structure of MoS₂ sheets.^{8,19} Although some studies, mostly through theoretical calculation,²⁰⁻²³ have shown these features have influence on electrical and optical properties of the monolayers, there are few studies on the effects of crystalline structures of MoS₂ on the performance of a device.^{11,24} The understanding of the influence of local lattice structures of monolayer TMDs at a device level would be great helpful to design high-performance devices towards practical applications. Herein, we report on how the post-treatments of the chemically exfoliated MoS₂ (ce-MoS₂) affect the local crystalline structures of MoS₂ sheets and in turn the device performance of organic solar cells (OSCs) where the 2D MoS₂ sheets are used as a hole extraction layer (HEL). With the optimization of local structures of MoS₂ sheets by oxygen incorporation, we could achieve 7.64% power conversion efficiency (PCE) of the OSCs, which is 53% higher than the OSCs with as-deposited ce-MoS₂ and comparable to the PCE (7.6%) of cells with standard poly(3,4-ethylenedioxythiophene):poly(styrenesulfonate) (PEDOT:PSS) as the HEL.

The ce-MoS₂ nanosheets and the solution-based thin film formations facilitate their use in devices such as OSCs.²⁵⁻²⁷ We synthesized the 2D MoS₂ sheets by lithium intercalation and exfoliation followed by the exhaustive dialysis.²⁸ The successful synthesis of ce-MoS₂ monolayers is evidenced through substantial

characterizations. A majority of the ce-MoS₂ sheets have a thickness of about 1 nm with lateral sizes of 200~300 nm, suggesting monolayers generated by the chemical method (Figure 1a-c).^{8,25} Compared to the powder X-ray diffraction (XRD) patterns for the bulk MoS₂ (Figure S1b), only the peak of (002) plane remained while the other peaks disappeared for the ce-MoS₂ sheets, which is mostly due to the fact that the MoS₂ sheets lied on the substrate with preferred orientation and the (002) plane is the thermodynamically stable planes.¹⁷ The broadening of (002) peak in the XRD pattern suggests the crystals with nanoscale sizes (Figure 1c) and the presence of disorder in the crystals as visualized by transmission electron microscopy (TEM) (Figure 1d and e). The Raman spectrum of the as-deposited ce-MoS₂ film (Figure S1c) shows two prominent peaks at 382 cm⁻¹ and 402 cm⁻¹ which corresponds to the in-plane E_{2g}¹ and out-of-plane A_{1g} modes of MoS₂, respectively.⁸ Compared to the peak positions at 384 cm⁻¹ and 403 cm⁻¹ and widths (typically 2-6 cm⁻¹) of a mechanically exfoliated monolayer, the slight peak shifts may be caused by the weak interlayer coupling due to the rotational stacking disorder of ce-MoS₂,^{8,24} and the broadening of E_{2g}¹ and A_{1g} peaks (~9 cm⁻¹) may be due to the thickness inhomogeneity of our film and the presence of defects.^{8,24} Furthermore, the TEM images clearly depicts the presence of various damages in the ce-MoS₂ sheets, including various edges, tears, pinholes, and amorphous-like feature (Figure 1b, d and e). An interplanar spacing of 0.27 nm measured from the top-view high-resolution TEM (HRTEM) image is consistent with the *d* spacing of (100) planes of hexagonal MoS₂.¹¹ The presence of many dislocations and distortions can also be revealed, as indicated by white circles in Figure 1d. Discontinuous crystal fringes along the sheet edges are observed from a few-layer sample in the side-view HRTEM image (Figure 1e).

Figure 2a shows the high angle annular dark field (HAADF) scanning transmission electron microscopy (STEM) image of ce-MoS₂ sheets. Despite the honeycomb crystalline order of MoS₂, we clearly observe disordered features, voids with various sizes, and irregular edges, suggesting abundant uncontrollable defects in the ce-MoS₂ sheets.^{19,28} High resolution HAADF STEM image in Figure 2b

reveals honeycomb lattice intensity variations of 2H-MoS₂ in various regions of the samples with high density of defects such as S vacancies as well as dislocations and different edge terminations.^{19,21} Such defective crystalline structures are believed to be a common feature of ce-MoS₂ sheets synthesized by chemical exfoliation methods due to the violent nature of the processes.¹⁹

Our OSCs³⁰⁻³² were fabricated using the ce-MoS₂ sheets as an HEL^{14,29,33} to investigate the influence of such local variations of crystalline structures on device performance. In state of the art OSCs, a layer of PEDOT:PSS, a conducting conjugated polymer, is commonly used as a standard interfacial material, *i.e.*, HEL, due to its suitable work function (~5.1 eV) for efficient hole extraction (energy level alignment) and exceptional solution processability (low-cost manufacture).^{34,35} However, the high acidity and hygroscopic features of PEDOT:PSS often make it implicated with the poor long-term stability of devices.³⁶ Here, we used ce-MoS₂ sheets (as-deposited, oxygen-incorporated, and thermal treated) to replace PEDOT:PSS layer. The device was comprised of an active blend of poly[[4,8-bis[(2-ethylhexyl)oxy]benzo[1,2-b:4,5-b']dithiophene-2,6-diyl][3-fluoro-2-[(2-ethylhexyl)carbonyl]thieno[3,4-b]thiophenediyl]] (PTB7) as donor and [6,6]-phenyl-C 71-butyric acid methyl ester (PC₇₁BM) as acceptor as shown in Figure 4a-b.³⁷ The ce-MoS₂ HEL was prepared by multiple-step of spin-coating from a 2 mg/mL solution (Figure S2). The thickness of the MoS₂ layers on the substrates was estimated to be about 2-3 nm (Figure S2) after spin-coating of 3 times.

We first examined the effect of phase compositions on device performance of the OSCs with the assumption of no change of other factors such as defects in the MoS₂ layer. It has been documented both theoretically and experimentally⁸ that ce-MoS₂ sheets consist of a mixture of two distinct phases (prismatic 2H and octahedral 1T) compared to 2H phase naturally in bulk MoS₂. The intercalation-induced phase transformation (from 2H to 1T) can be reversed *via* mild annealing such that the semiconducting properties of the pristine MoS₂ can be restored.⁸ We found that the as-prepared ce-MoS₂

is predominantly in 1T phase, reaching 88.5% calculated from the X-ray photoelectron spectroscopy (XPS) measurement (Figure S4 and S5). After annealing the ce-MoS₂ thin films at 150 °C and 300 °C for 10 min in a glovebox, the percentage of the 2H phase in the ce-MoS₂ thin films increased to 89% and almost 100%, respectively. The PCE of the OSCs, in which the active layer was deposited on the as-deposited ce-MoS₂ layer, is 4.99%. However, the PCE of the OSCs varied randomly while increasing the 2H phase by annealing ce-MoS₂ at different temperatures, *i.e.*, the PCE of the OSCs reduced from 5.77% to 4.77% while increasing the 2H phase from 89% to 100% (Figure S6, Table S1). Although the change of the device performance is not in line with the percentage of 2H phase contained in the ce-MoS₂ thin films, the results suggest that the phase composition has an effect on the hole extraction properties of ce-MoS₂ in the OSCs.

As observed in the TEM images, there are many crystalline structural defects, such as S vacancies, in the ce-MoS₂ sheets,^{10,19,24} thus we could expect that the filling of such S vacancies can remove the-defect-induced levels in the band-gap²⁰⁻²³ of the MoS₂ and in turn reduce trapping possibility of the free carriers separated from excitons and facilitate transport and collection of the carriers in OSCs.³⁸ On the other hand, it is well known that interfacial engineering is a prominent way to enhance the performance of OSCs, controlling hole and electron extractions and collections.³⁹⁻⁴² Hence, we developed a simple strategy to produce oxygen-incorporated ce-MoS₂ (O-ce-MoS₂) in order to tailor its structural and electrical properties. The O-ce-MoS₂ layer was obtained by 3 min UV-ozone treatment on ce-MoS₂ ultrathin films. We found by XPS measurements that oxygen (O) atoms penetrated into the ce-MoS₂ crystal lattices after UV-ozone treatment, which might partially fill the S vacancies. The O incorporation could passivate the structural defects as schematized in Figure 3a (also see Figure S7) and led to a change of interfacial energy level alignment.

After O incorporation, the normalized peak intensity of O1s in the XPS spectra was increased (Figure 3b). The O1s peak was de-convoluted to two peaks at 532 and 530.6 eV (Figure 3c), which are ascribed to adsorbed oxygen and lattice oxygen, respectively.⁴³ The increase in intensity of the 530.6 eV peak for O-ce-MoS₂ suggests the successful incorporation of O atoms into the MoS₂ crystal lattices. The Mo3d, S2s, and S2p core level peaks in Figure 3d further suggest that the stoichiometric structure and phase composition for the MoS₂ films mostly remained unchanged after the O incorporation. Notably, the peaks observed at about 236 eV, corresponding to Mo⁶⁺, were with percentage of 7.4% in the ce-MoS₂ (Figure 3d), partially due to the oxidation of Mo during synthesis. After the O incorporation, the Mo⁶⁺ content was increased to 12.8%. The additional 5.4% Mo⁶⁺ may arise from both the slight oxidation and more possibly the electron delocalized from Mo to filled O in O-ce-MoS₂. It should be noted that this short time UV-ozone treatment (3 min) did not fully oxidize the MoS₂ into MoO₃ as confirmed by Raman and photoluminescence (PL) spectra before and after the UV-ozone treatment (Figures S8-S9). The retaining of the E¹_{2g} and A_{1g} peaks and PL properties rule out the possibilities of complete conversion from MoS₂ to MoO₃.

The photocurrent-voltage (*J-V*) curves of the OSCs fabricated using the as-deposited ce-MoS₂ and O-ce-MoS₂ layers are shown in Figure 4d, with relevant parameters summarized in Table 1. The device with ce-MoS₂ as HEL has a PCE of 4.99% with an open circuit voltage (*V*_{OC}), short-circuit current (*J*_{SC}), and fill factor (FF) of 0.62 V, 14.29 mA cm⁻², and 0.563, respectively. By comparison, the device where O-ce-MoS₂ was used as the HEL had a significant enhancement in the PCE of 7.64% (53% enhancement) with *V*_{OC}, *J*_{SC}, and FF of 0.73 V, 14.98 mA cm⁻², and 0.699, respectively. This efficiency is comparable to that of the solar cells with standard PEDOT:PSS (7.60%) as the HEL. The enhancement in the device performance by using the O-ce-MoS₂ as a HEL layer could be attributed to the incorporation of oxygen atoms into the lattices, which led to the possible filling of the vacancies and the increase in the work function (WF) of the O-ce-MoS₂.

To examine the effect of local structural defects on the device performance, we studied the PL properties of the PTB7 active material used in our OSCs. The PTB7 film was deposited on top of the ce-MoS₂ or O-ce-MoS₂ ultrathin films. As shown in Figure 4f, the PL intensity of PTB7 on the ce-MoS₂ layer is much lower than that on the O-ce-MoS₂ layer. The PL quenching is believed to be mostly due to the local structural defects of ce-MoS₂ as observed in the TEM images (Figures 1 and 2), which could act as a non-irradiation recombination center to quench the PL of PTB7. The existence of S vacancies could cause unsaturated electrons of the surrounding Mo atoms and act as electron donors to make the MoS₂ electron rich as experimentally observed previously.²¹ The presence of the S vacancies could introduce deep donor defect states in the band-gap.²¹ This result suggests that our UV-ozone treatment is an efficient approach to modify the structures of the ce-MoS₂ sheets and thus the performance of our OSCs was improved. The oxygen atoms might be incorporated at the defective sites of the ce-MoS₂ sheets, though further direct visualization of such oxygen atoms is need. Efforts have been taken to justify the incorporation of oxygen atoms into the defects using STEM, however, we are not successful till now.

We measured the ultraviolet photoelectron spectroscopy (UPS) of the ce-MoS₂ and O-ce-MoS₂ sheets to confirm the WF change after O incorporation into the lattices, which significantly influences device performance. As shown in the Figures 4h-4i, the WF of the MoS₂ increased from about -4.50 eV to -4.93 eV after O incorporation. The mismatch between the WF of ce-MoS₂ and the HOMO of PTB7 limited the build-up of V_{oc} . V_{oc} is normally governed by the energy levels of the donor and acceptor materials in case of Ohmic contacts.^{34,35} Unlike the formation of Ohmic contact between PEDOT:PSS and PTB7, the ce-MoS₂ formed a Schottky contact with PTB7 layer. The poor electrical contact between ce-MoS₂ and PTB7 could seriously deteriorate the device performance. In the case of O-ce-MoS₂, the defect-induced states could be reduced due to the possible filling the of S vacancies with O atoms, and in turn the Fermi level shifted down away from the minima of the conduction band minimum (normally MoS₂ sheets exhibit *n*-type semiconductor behavior.) because of the lower concentration of electron donors. The

enhanced WF is beneficial for the Ohmic contact with the donor materials (Figure 4i). As a consequence, a striking enhancement of the V_{oc} was achieved and this led to improvement of in the PCE of the O-ce-MoS₂ as compared to the ce-MoS₂.

Furthermore, from the external quantum efficiency (EQE) spectra (Figure 4e), we clearly see that the photocurrent of the device with the O-ce-MoS₂ layer was enhanced significantly as compared to the OSC with ce-MoS₂, which is consistent with the change in J_{sc} . This current enhancement directly related to the reduction of structural defects in the O-ce-MoS₂ layer which facilitated the carrier transport and the better match of energy levels between the O-ce-MoS₂ and ITO electrode which improved carrier injection at the interfaces and collection by the ITO anode. We calculated the series resistance (R_s) of these devices from the dark $J-V$ curves. Compared to the device with the ce-MoS₂, the R_s value of device with the O-ce-MoS₂ decreased from 4.03 to 1.88 Ωcm^2 (Table 1). The reduction of R_s suggests a higher conductivity of the O-ce-MoS₂ film and the FF was enhanced. To compare the charge collection between the devices with ce-MoS₂ and O-ce-MoS₂, the charge collection probability (P_C)⁴⁴ with respect to the internal voltage (V_{int}) under illumination at 100 mW cm^{-2} was calculated as shown in Figure 4g. It shows that the P_C of the device based on O-ce-MoS₂ is higher than that based on ce-MoS₂ in the full range from short-circuit to open-circuit conditions.⁴³ The P_C increased from 90.9% to 97.5% under the short-circuit condition, indicating an increase in charge collection originated from the oxygen incorporation.

In conclusion, our study of various local crystalline structures in ce-MoS₂ sheets provides new insights into how these local characteristics affect the device performance and approaches on how to tailor the local characteristics towards high-performance devices. Despite the difficulty in synthesizing perfect crystals of 2D TMDs, we showed UV-ozone post-treatment is an efficient method for improving the electronic properties of MoS₂ sheets used in OSCs. The incorporation of oxygen atoms into the ce-MoS₂ lattices could reduce defects and tuned the electronic properties of the ce-MoS₂ in a manner of doping or

alloy form. Our results demonstrate that ce-MoS₂ ultrathin film is an alternative HTL material to develop high-efficiency OSCs with compatibility for a flexible and solution-based process. The knowledge developed in our study could help to optimize the performance of 2D TMDs in general and to pave the way towards practical applications of these novel nanomaterials.

Acknowledgements

This work was supported by the National Basic Research Program (2014CB643503, 2014CB932500) and the National Natural Science Foundation of China (Grants Nos. 91233114, 51261130582, and 50990063, 51222202). M. Xu thanks Zhejiang Provincial Natural Science Foundation of China (Youth Talent Program: R4110030), the Program for New Century Excellent Talents in University (NCET-12-0494), the Research Fund for the Doctoral Program of Higher Education (20130101110123) and the Program for 14th China-Japan S&T Cooperation (2013DFG52800). C. Jin is partly supported by the Program for Innovative Research Team in University of Ministry of Education of China (IRT13037). The work on microscopy was carried out in Centre of Electron Microscopy of Zhejiang University. X. Yang thanks Tao Liang for Raman test. X. Yang and W. Fu contributed equally to this work.

Notes and references

^a State Key Laboratory of Silicon Materials, MOE Key Laboratory of Macromolecular Synthesis and Functionalization, Department of Polymer Science and Engineering, Zhejiang University, Hangzhou 310027, P. R. China

E-mails: hzchen@zju.edu.cn, msxu@zju.edu.cn

^b State Key Laboratory of Polymer Physics and Chemistry, Changchun Institute of Applied Chemistry, Changchun 130022, P. R. China

^c State Key Laboratory of Silicon Materials, Key Laboratory of Advanced Materials and Applications for Batteries of Zhejiang Province, Department of Materials Science and Engineering, Zhejiang University, Hangzhou, Zhejiang 310027, P. R. China

^d State Key Laboratory of Silicon Materials and Department of Materials Science and Engineering, Zhejiang University, Hangzhou 310027, China

‡ These authors contributed equally.

Electronic Supplementary Information (ESI) available: Experimental procedures, characterization details and photovoltaic characteristics of solar cells. See DOI:10.1039/c000000x/

- 1 M. S. Xu, T. Liang, M. M. Shi and H. Z. Chen, *Chem. Rev.*, 2013, **113**, 3766.
- 2 M. Chhowalla, H. S. Shin, G. Eda, L. J. Li, K. P. Loh and H. Zhang, *Nature Chem.*, 2013, **5**, 263.
- 3 S. Z. Butler, S. M. Hollen, L. Y. Cao, Y. Cui, J. A. Gupta, H. R. Gutiérrez, T. F. Heinz, S. S. Hong, J. X. Huang, A. F. Ismach, E. Johnston-Halperin, M. Kuno, V. V. Plashnitsa, R. D. Robinson, R. S.

- Ruoff, S. Salahuddin, J. Shan, L. Shi, M. G. Spencer, M. Terrones, W. Windl and J. E. Goldberger, *ACS Nano*, 2013, **7**, 2898.
- 4 Q. H. Wang, K. Kalantar-Zadeh, A. Kis, J. N. Coleman and M. S. Strano, *Nature Nanotech.*, 2012, **7**, 699.
- 5 J. N. Coleman, M. Lotya, A. O' Neill, S. D. Bergin, P. J. King, U. Khan, K. Young, A. Gaucher, S. De, R. J. Smith, I. V. Shvets, S. K. Arora, G. Stanton, H. -Y. Kim, K. Lee, G. T. Kim, G. S. Duesberg, T. Hallam, J. J. Boland, J. J. Wang, J. F. Donegan, J. C. Grunlan, G. Moriarty, A. Shmeliov, R. J. Nicholls, J. M. Perkins, E. M. Grieverson, K. Theuwissen, D. W. McComb, P. D. Nellist and V. Nicolosi, *Science*, 2011, **331**, 568.
- 6 B. Radisavljevic, A. Radenovic, J. Brivio, V. Giacometti and A. Kis, *Nature Nanotech.*, 2011, **6**, 147.
- 7 A. Splendiani, L. Sun, Y. B. Zhang, T. S. Li, J. Kim, C. -Y. Chim, G. Galli and F. Wang, *Nano Lett.*, 2010, **10**, 1271.
- 8 G. Eda, H. Yamaguchi, D. Voiry, T. Fujita, M. W. Chen and M. Chhowalla, *Nano Lett.*, 2011, **11**, 5111.
- 9 M. Chhowalla and G. A. J. Amaratunga, *Nature*, 2000, **407**, 164.
- 10 D. Voiry, M. Salehi, R. Silva, T. Fujita, M. W. Chen, T. Asefa, V. B. Shenoy, G. Eda and M. Chhowalla, *Nano Lett.*, 2013, **13**, 6222.
- 11 J. F. Xie, H. Zhang, S. Li, R. X. Wang, X. Sun, M. Zhou, J. F. Zhou, X. Wen (David) Lou and Y. Xie, *Adv. Mater.*, 2013, **25**, 5807.
- 12 M. A. Lukowski, A. S. Daniel, F. Meng, A. Forticaux, L. S. Li and S. Jin, *J. Am. Chem. Soc.*, 2013, **135**, 10274.
- 13 M. Bernardi, M. Palummo and J. C. Grossman, *Nano Lett.*, 2013, **13**, 3664.

- 14 X. Gu, W. Cui, H. Li, Z. W. Wu, Z. Y. Zeng, S. T. Lee, H. Zhang and B. Q. Sun, *Adv. Energy Mater.*, 2013, **3**, 1262.
- 15 R. S. Sundaram, M. Engel, A. Lombardo, R. Krupke, A. C. Ferrari, P. vouris and M. Steiner, *Nano Lett.*, 2013, **13**, 1416.
- 16 N. Perea-López, A. L. Elías, A. Berkdemir, A. Castro-Beltran, H. R. Gutiérrez, S. Feng, R. Lv, T. Hayashi, F. López-Urías, S. Ghosh, B. Muchharla, S. Talapatra, H. Terrones and M. Terrones, *Adv. Funct. Mater.*, 2013, **23**, 5511.
- 17 Z. Y. Zeng, Z. Y. Yin, X. Huang, H. Li, Q. Y. He, G. Lu, F. Boey and H. Zhang, *Angew. Chem. Int. Ed.*, 2011, **50**, 11093.
- 18 P. Joensen, R. F. Frindt and S. R. Morrison, *Mater. Res. Bull.*, 1986, **21**, 457.
- 19 G. Eda, T. Fujita, H. Yamaguchi, D. Voiry, M. W. Chen and M. Chhowalla, *ACS Nano.*, 2012, **6**, 7311.
- 20 W. Zhou, X. L. Zou, S. Najmaei, Z. Liu, Y. M. Shi, J. Kong, J. Lou, P. M. Ajayan, B. I. Yakobson and J. C. Idrobo, *Nano Lett.*, 2013, **13**, 2615.
- 21 H. Qiu, T. Xu, Z. L. Wang, W. Ren, H. Y. Nan, Z. H. Ni, Q. Chen, S. J. Yuan, F. Miao, F. Q. Song, G. Long, Y. Shi, L. T. Sun, J. L. Wang and X. R. Wang, *Nature Commun.*, 2013, **4**, 2642.
- 22 A. M. van der Zande, P. Y. Huang, D. A. Chenet, T. C. Berkelbach, Y. M. You, G. -H. Lee, T. F. Heinz, D. R. Reichman, D. A. Muller and J. C. Hone, *Nature Mater.*, 2013, **12**, 554.
- 23 H. P. Komsa, S. Kurasch, O. Lehtinen, U. Kaiser and A. V. Krasheninnikov, *Phys. Rev. B*, 2013, **88**, 035301.
- 24 D. Voiry, H. Yamaguchi, J. W. Li, R. Silva, D. C. B. Alves, T. Fujita, M. W. Chen, T. Asefa, V. B. Shenoy, G. Eda and M. Chhowalla, *Nature Mater.*, 2013, **12**, 850.
- 25 H. S. S. R. Matte, A. Gomathi, A. K. Manna, D. J. Late, R. Datta, S. K. Pati and C. N. R. Rao, *Angew. Chem. Int. Ed.*, 2010, **49**, 4059.

- 26 G. L. Frey, K. J. Reynolds and R. H. Friend, *Adv. Mater.*, 2002, **14**, 265.
- 27 G. L. Frey, K. J. Reynolds, R. H. Friend, H. Cohen and Y. Feldman, *J. Am. Chem. Soc.*, 2003, **125**, 5998.
- 28 S. S. Chou, M. De, J. Kim, S. Byun, C. Dykstra, J. Yu, J. X. Huang and V. P. Dravid, *J. Am. Chem. Soc.*, 2013, **135**, 4584.
- 29 S. Kato, R. Ishikawa, Y. Kubo, H. Shirai and K. Ueno, *Jap. J. Appl. Phys.*, 2011, **50**, 071604.
- 30 X. Yang, C. C. Chueh, C. Z. Li, H. L. Yip, P. P. Yin, H. Z. Chen, W. C. Chen and A. K. Y. Jen, *Adv. Energy Mater.*, 2013, **3**, 666.
- 31 W. F. Fu, Y. Shi, L. Wang, M. M. Shi, H. Y. Li and H. Z. Chen, *Solar Energy Materials & Solar Cells*, 2013, **117**, 329.
- 32 Y. Z. Lin, H. J. Fan, Y. F. Li and X. W. Zhan, *Adv. Mater.*, 2012, **24**, 3087.
- 33 J. M. Yun, Y. J. Noh, J. S. Yeo, Y. J. Go, S. I. Na, H. G. Jeong, J. Kim, S. Lee, S. S. Kim, H. Y. Koo, T. W. Kim and D. Y. Kim, *J. Mater. Chem. C*, 2013, **1**, 3777.
- 34 L. T. Dou, J. B. You, Z. R. Hong, Z. Xu, G. Li, R. A. Street and Y. Yang, *Adv. Mater.*, 2013, **25**, 6642.
- 35 A. J. Heeger, *Adv. Mater.*, **2013**, doi: 10.1002/adma.201304373.
- 36 J. Liu, Y. H. Xue, Y. X. Gao, D. S. Yu, M. Durstock and L. M. Dai, *Adv. Mater.*, 2012, **24**, 2228.
- 37 Z. C. He, C. M. Zhong, S. J. Su, M. Xu, H. B. Wu and Y. Cao, *Nature Photonics*, 2012, **6**, 591.
- 38 S. Chen, C. E. Small, C. M. Amb, J. Subbiah, T. Lai, S. W. Tsang, J. R. Manders, J. R. Reynolds and F. So, *Adv. Energy Mater.*, 2012, **2**, 1333.
- 39 H. L. Yip, A. K. Y. Jen, *Energy Environ. Sci.*, 2012, **5**, 5994.
- 40 J. J. Li, L. J. Zuo, H. B. Pan, H. Jiang, T. Liang, Y. Shi, H. Z. Chen and M. S. Xu, *J. Mater. Chem. A*, 2013, **1**, 2379.

- 41 Z. Tan, L. Li, F. Wang, Q. Xu, S. Li, G. Sun, X. Tu, X. Hou, J. Hou and Y. Li, *Adv. Energy Mater.*, 2014, **4**, 1.
- 42 S. J. Liu, K. Zhang, J. M. Lu, J. Zhang, H. L. Yip, F. Huang and Y. Cao, *J. Am. Chem. Soc.*, 2013, **135**, 15326.
- 43 K. J. Carroll, J. U. Reveles, M. D. Shultz, S. N. Khanna, E. E. Carpenter, *Journal of Physical Chemistry C*, 2011, **115**, 2656.
- 44 A. K. K. Kyaw, D. H. Wang, D. Wynands, J. Zhang, T. Q. Nguyen, G. C. Bazan and A. J. Heeger, *Nano Lett.*, 2013, **13**, 3796.

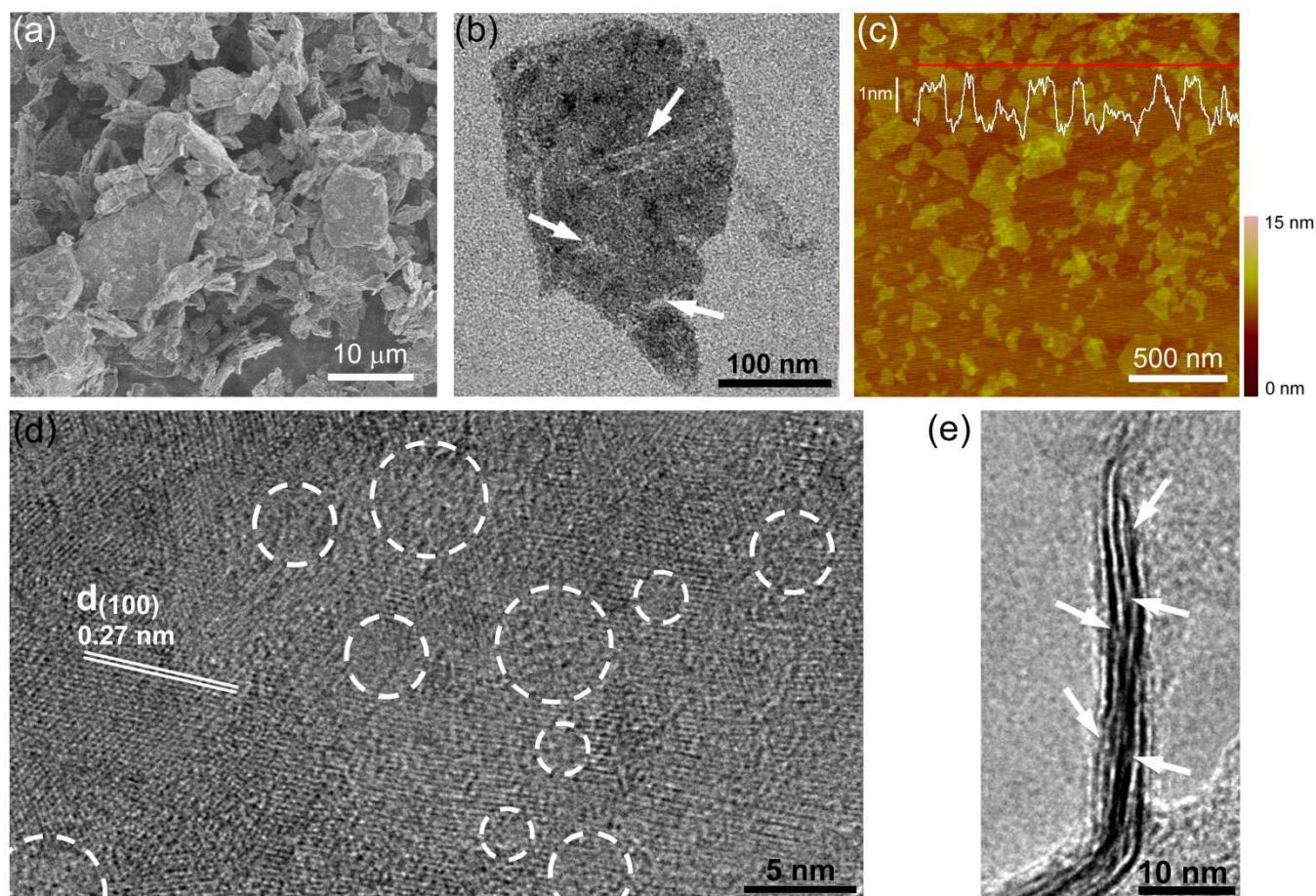


Figure 1. Local structure characteristics of ce-MoS₂ sheets. (a) Scanning electron microscopy (SEM) image of commercial MoS₂ powder. The MoS₂ powder has sizes from few to tens of micrometers and thickness of few micrometers. (b) Transmission electron microscopy (TEM), obviously showing the presence of internal edges (tears and pinholes) of ce-MoS₂ induced by the Li intercalation reaction. (c) Atomic force microscopy (AFM) images of ce-MoS₂ nanosheets deposited on SiO₂/Si substrate. (d) Top-view high resolution TEM (HRTEM) image of ce-MoS₂ nanosheet. The white dash-circles highlight dislocations and distortions of the crystals. (e) Side-view HRTEM image of a few-layer ce-MoS₂ nanosheet, revealing discontinuous crystal fringes along the sheet edges. These observations suggest existence of local structural defects of the ce-MoS₂ sheets.

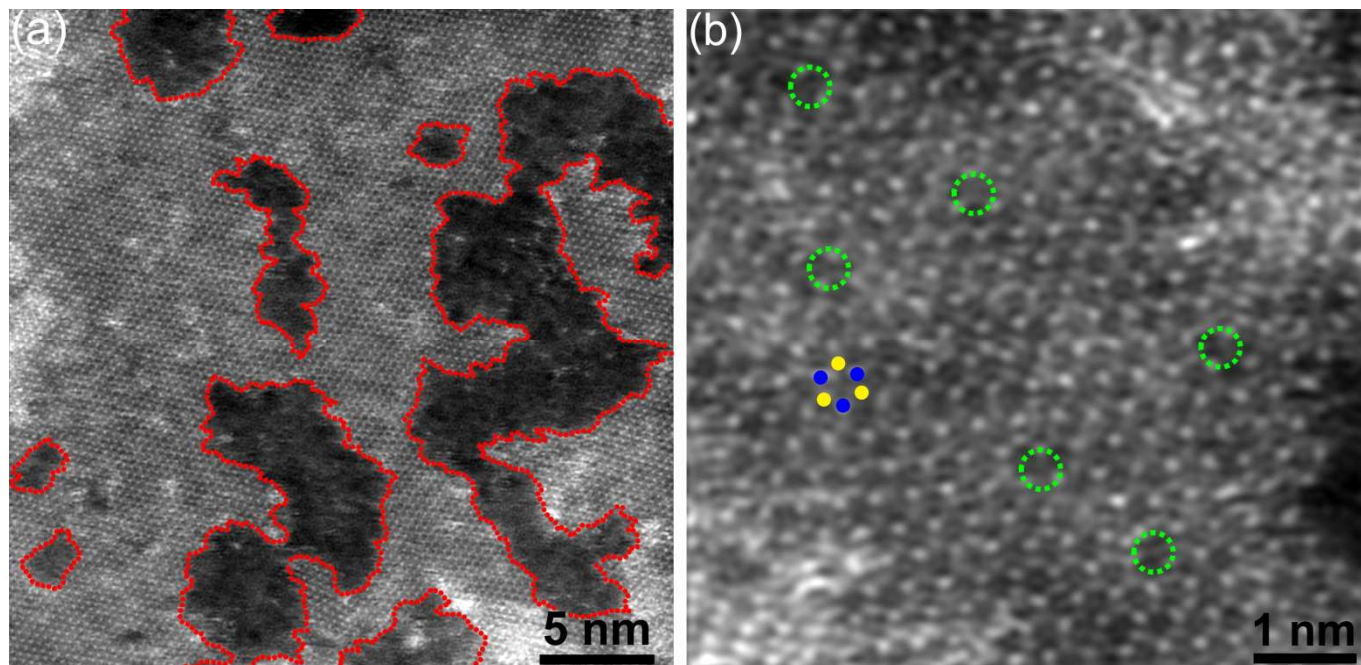


Figure 2. HAADF STEM images of ce-MoS₂ sheets. (a) The image clearly shows irregular edges and pinholes with various sizes, indicating abundant uncontrollable defects in a typical ce-MoS₂ sheet. (b) The high resolution image shows individual Mo and S atoms (represented by blue and yellow balls in the image, respectively), their honeycomb arrangement, and local crystalline defects. Such structural defects include S vacancies whose positions are shown with green dash-circles, dislocations, and different edge terminates.

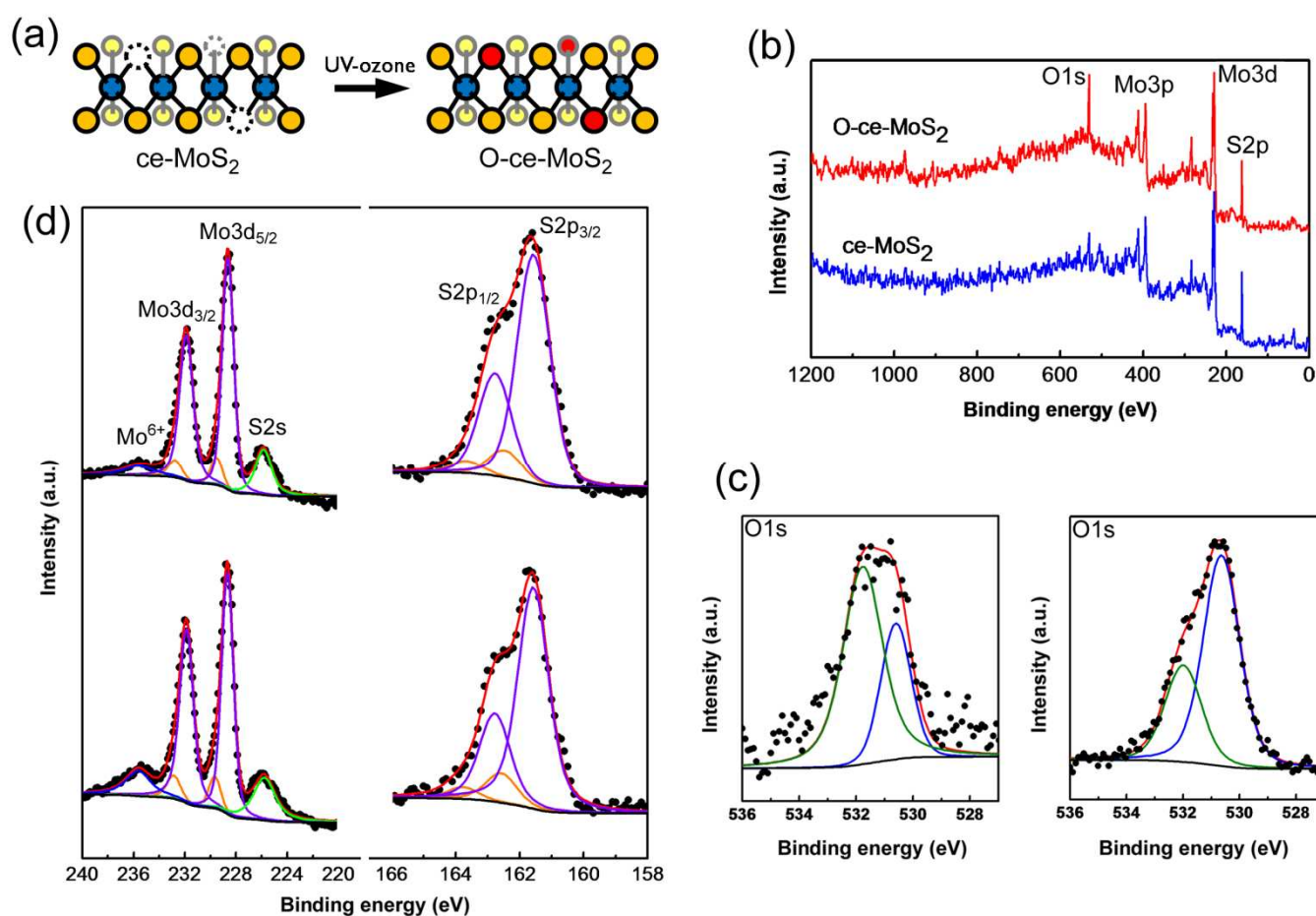


Figure 3. Chemical characterization of MoS₂ sheets before and after oxygen incorporation. (a) Schematic of production of O-ce-MoS₂ from ce-MoS₂. (b) Whole XPS spectra of ce-MoS₂ and O-ce-MoS₂. The O1s to Mo3d ratios are calculated to be 0.768 and 0.988 before and after ozone treatment, respectively. The relative change of the atomic concentrations of the O1s and Mo3d, *i.e.*, the increased O ratio after the treatment suggests the successful incorporation of O atoms. (c) XPS spectra showing O1s core level peaks of ce-MoS₂ (left panel) and O-ce-MoS₂ (right panel). The O1s peak was de-convoluted to two peaks at 532 eV and 530.6 eV, which are ascribed to adsorbed oxygen and lattice oxygen, respectively. (d) XPS spectra showing Mo3d, S2s, and S2p core level peaks of ce-MoS₂ (upper panel) and O-ce-MoS₂ (lower panel). After Shirley background subtraction, the Mo3d and S2p peaks were de-convoluted to show the 2H and 1T contributions, represented by orange and violet plots, respectively.

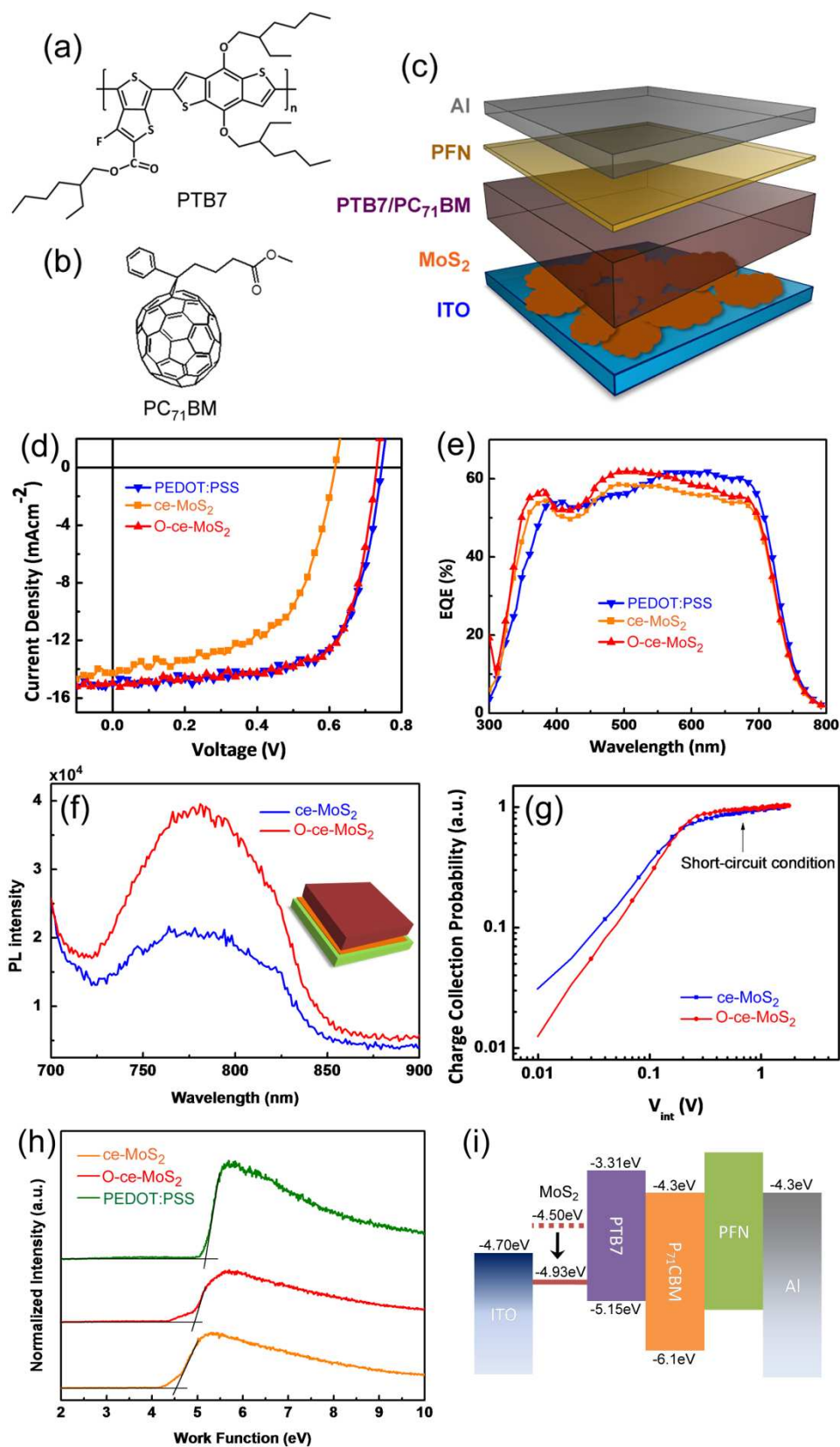


Figure 4. Organic solar cells with MoS₂ sheets as the hole extraction layer. Chemical structures of (a) PTB7 and (b) PC₇₁BM used in our solar cells. (c) Schematic of the device architecture. (d) *J-V*

characteristics and (e) external quantum efficiency (EQE) spectra of the OSC devices with PEDOT:PSS, ce-MoS₂, and O-ce-MoS₂ as HELs, respectively, under AM 1.5G illumination (100 mW cm⁻²). (f) The steady-state photoluminescence spectra of PTB7 film deposited on ce-MoS₂ and O-ce-MoS₂ thin films on a quartz substrate, respectively. The excitation light is incoming from the MoS₂ side (quartz side) in order to easily observe PL quenching induced by the MoS₂ defects. (g) Charge collection probability as a function of internal voltage for devices based on ce-MoS₂ and O-ce-MoS₂ HELs. (h) Ultraviolet photoemission spectra (UPS) of ce-MoS₂, O-ce-MoS₂, and PEDOT:PSS deposited on ITO substrates. (i) Energy diagram of PTB7:PC₇₁BM active layer sandwiched between ITO anode and Al cathode utilizing ce-MoS₂ and O-ce-MoS₂ as the hole extraction layer, respectively. Oxygen incorporation can increase the work function of ce-MoS₂ from -4.50 eV to -4.93 eV.

Table 1. Performance of the OSC devices with PEDOT:PSS, ce-MoS₂, and O-ce-MoS₂ as hole extraction layers, respectively, under AM 1.5G illumination (100 mW cm⁻²).

Anode buffer layer	Treatment	Voc [V]	Jsc [mA cm ⁻²]	FF	PCE [%]	Rs [Ω cm ²]
PEDOT:PSS	Annealing	0.74	15.00	0.685	7.60	2.53
ce-MoS ₂	No Annealing	0.62	14.29	0.563	4.99	4.03
O-ce-MoS ₂	No Annealing	0.73	14.98	0.699	7.64	1.88

ToC figure

